

## Crystallization Kinetics in Microphase-Separated Poly(ethylene oxide)-*block*-poly(1,4-butadiene)

Hsin-Lung Chen,<sup>\*,†</sup> Ja-Chi Wu,<sup>†</sup> Tsang-Lang Lin,<sup>‡</sup> and J. S. Lin<sup>§</sup>

Department of Chemical Engineering, National Tsing Hua University, Hsin-Chu, Taiwan 30013, R.O.C.; Department of Engineering and System Science, National Tsing Hua University, Hsin-Chu, Taiwan 30013, R. O. C.; and Solid State Division, Oak Ridge National Laboratory, Oak Ridge, Tennessee 37831

Received April 2, 2001; Revised Manuscript Received June 11, 2001

**ABSTRACT:** We studied the crystallization kinetics in a diblock copolymer system exhibiting different mesophase structures in the melt. A symmetric poly(ethylene oxide)-*block*-poly(1,4-butadiene) (PEO-*b*-PB) was blended with a low molecular weight PB homopolymer to yield the block copolymer blends containing lamellar, cylindrical, and spherical PEO microdomains. The crystallization kinetics of PEO blocks in these nanoscaled microdomains was then studied by monitoring the development of crystallinity in the course of isothermal crystallization. In the lamellar melt, crystallization could occur at the normal undercooling, and its kinetics closely followed the classical Avrami model found in the spherulitic crystallization of homopolymers. Crystallinity developments in the cylindrical and spherical morphology obeyed a simple exponential function prescribed by the first-order kinetics. This first-order kinetic behavior along with the exceedingly large undercooling verified the homogeneous nucleation controlled kinetics in these two types of mesophases. Crystallization in the lamellar melt transformed the melt structure into a highly interconnected lamellar morphology due to the ability of the crystal growth fronts to repeatedly thrust into the microdomains yet to be crystallized. For the crystallization condition chosen (i.e., cooling at  $-5$  °C/min from the melt), the melt structures associated with the cylindrical and spherical morphology were not totally disrupted and transformed into one-dimensionally stacked lamellae upon crystallization. The melt mesophases were not fully preserved either, suggesting that some intermediate structures may have been formed through the crystallization.

### Introduction

Crystalline–amorphous (C–A) block copolymers form a special class of materials exhibiting two self-organizing mechanisms driven by crystallization and interblock incompatibility (microphase separation). Below the order–disorder transition temperature ( $T_{ODT}$ ), crystallization in C–A block copolymers may take place within an existent mesophase templated by the prior microphase separation, where the process can be divided into the following cases:

Case 1. Crystallization in the three-dimensionally (3-D) continuous phase: The C block accounts for the major component in the system, so that it forms a 3-D continuous phase in the melt. Crystallization in this continuous matrix is analogous to that in the homopolymers in the sense that the crystal growth may propagate continuously over a macroscopic length scale.

Case 2. Crystallization within the nanoscaled microdomains: When the two components are of similar proportion or when the C block becomes the minor constituent, microphase separation in the melt state may generate various types of long-range ordered microdomains consisting of the C blocks. Lamellar, cylindrical, and spherical microdomains have typically been formed depending on the composition of system.<sup>1–4</sup> These microdomain patterns may impose nanoscaled confinement to frustrate the crystal growth and thus

serve as the templates for studying the effect of spatial confinement on the crystallization behavior of chain molecules.

Most studies of C–A block copolymers have focused on case 2, and several intriguing features have been disclosed so far. For instance, crystallization within the microdomains would require the introduction of an equilibrium degree of chain folding,<sup>5,6</sup> in contrast to the kinetically introduced chain folding in homopolymer crystallization; the melt mesophase may sometimes be perturbed by crystallization of the C minority blocks, and the extent of perturbation is governed by the driving forces of crystallization and microphase separation as well as the  $T_g$  of the corona A blocks.<sup>7–12</sup>

In addition to the structural patterns, the crystallization kinetics of C–A block copolymers also exhibits one feature not seen in the conventional crystallization of homopolymers in that the overall kinetics may be dominated by the homogeneous nucleation in the microdomains.<sup>13–18</sup> The nucleation is potentially homogeneous because the macroscopic impurity particles cannot be effectively contained within the nanoscaled microdomains to serve as the heterogeneous nuclei. In the previous crystallization studies of poly(ethylene oxide) (PEO)–polyisoprene (PI) block copolymers, Robitaille et al.<sup>14</sup> and Schnablegger et al.<sup>15</sup> showed that very large undercoolings were required to initiate the crystallizations, implying that homogeneous nucleations were operative in the PEO microdomains. Recently, Loo et al. revealed the direct evidence of a homogeneous nucleation-controlled crystallization in a polyethylene-*block*-(styrene-*ran*-ethylene-*ran*-butene) (E/SEB) through time-resolved WAXS study.<sup>17</sup> The development of crystallinity during isothermal crystallization in the spheri-

<sup>†</sup> Department of Chemical Engineering, National Tsing Hua University.

<sup>‡</sup> Department of Engineering and System Science, National Tsing Hua University.

<sup>§</sup> Oak Ridge National Laboratory.

\* To whom correspondence should be addressed.

cal microdomains was found to follow first-order kinetics which indicated that the rate of isothermal crystallization was simply proportional to the fraction of spheres yet to be crystallized, as anticipated for a process controlled by homogeneous nucleation.

It should be noted that homogeneous nucleation-controlled crystallization is by no means universal among the C-A systems containing C minority blocks. In many instances, crystallization still proceeds through a mechanism analogous to the spherulitic crystallization of homopolymers. Nojima et al. have studied the crystallization behavior of polycaprolactone (PCL) minority blocks in PCL-*block*-polybutadiene (PCL-*b*-PB).<sup>8,19,20</sup> The crystallization kinetics was found to consistently follow the classical Avrami equation with the Avrami exponent ( $n$ ) comparable to that of PCL homopolymer. Ryan et al. investigated the development of crystalline structure in PE-*block*-poly(ethylene) and PE-*block*-poly(ethylene-propylene).<sup>10</sup> Crystallization of the PE blocks from both lamellar and cylindrical microdomains displayed an Avrami exponent ( $n = 3.0 \pm 0.1$ ) typical to the spherulitic crystallization process. The reason that crystallizations in these systems were not dominated by homogeneous nucleation was probably due to the ability of the crystallization process to effectively disrupt the original mesophase in the melt. The crystallization in this case could proceed as if the spatial discontinuity of the microdomains did not exist to prevent the crystal growth from propagating over a macroscopic length scale (further discussion will be presented later).

In a prior brief report, we have studied the crystallization kinetics of PEO minority blocks in PEO-*b*-PB/PB blends.<sup>18</sup> A symmetric PEO-*b*-PB was blended with a low molecular weight PB homopolymer to yield the block copolymer blends containing lamellar, cylindrical, and spherical PEO microdomains in the melt state. The crystallization kinetics of PEO blocks in these microdomain patterns was then studied by the cooling experiment, and a distinct correlation between the kinetics and the microdomain morphology was identified. In the present study, we proceed further to explore the crystallization mechanism in each mesophase structure through monitoring the crystallinity development in the course of isothermal crystallization. It will be shown that the crystallinity developments in cylindrical and spherical morphology are properly described by the first-order kinetics previously observed in E/SEB,<sup>17</sup> while the kinetics in the lamellar melt closely follows a pattern similar to the spherulitic crystallization of homopolymers. Since the perturbation of melt morphology may closely connect with the crystallization kinetics, the crystalline morphology of PEO-*b*-PB/PB blends is also probed and discussed in line with the observed kinetic behavior.

## Experimental Section

The symmetric PEO-*b*-PB with the polydispersity index  $M_w/M_n = 1.04$  was synthesized by sequential anionic polymerization of butadiene and ethylene oxide (Polymer Source, Inc.).  $M_n$  of the PEO and PB blocks was 6000 and 5000, respectively, which prescribed the volume fraction of PB  $f_{PB} = 0.50$ . The 1,4-addition PB homopolymer with  $M_n = 1000$  and  $M_w/M_n = 1.13$  was also synthesized by anionic polymerization (Polymer Source, Inc.). PEO-*b*-PB/PB blends were prepared by solution mixing. PEO-*b*-PB and PB were dissolved in chloroform at room temperature (ca. 25 °C), yielding 1 wt % solution. The microphase-separated blends were obtained after removing most of the solvent on a hot plate at 60 °C followed by drying in vacuo at 50 °C for 2 h.

Small-angle X-ray scattering (SAXS) was utilized to probe the morphology of amorphous and crystalline PEO-*b*-PB/PB blends. The amorphous samples were prepared by first annealing at 80 °C ( $T_m$  of PEO < 80 °C <  $T_{ODT}$ ;  $T_{ODT} > 150$  °C) for 5 min followed by cooling to room temperature. The SAXS measurements were performed at 60 °C for the blends with the overall volume fraction of PB  $f_{PB} = 0.64$  since the PEO blocks in these compositions crystallized upon cooling to room temperature. For the blends with  $f_{PB} = 0.69$ , the SAXS profiles were collected at room temperature because the PEO blocks remained amorphous after cooling to room temperature due to extremely slow crystallization rate. (The PEO blocks actually never crystallized even after storage at room temperature for 2 months.)

As for the characterization of the crystalline morphology, the samples were prepared by cooling from 80 to -50 °C at -5 °C/min followed by annealing at -50 °C for 30 min. The degree of crystallinity in terms of the weight of crystals per unit weight of PEO was over 0.75, irrespective of blend compositions. The SAXS characterizations of all crystalline samples were conducted at room temperature.

The X-ray source of SAXS, an 18 kW rotating anode X-ray generator (Rigaku) equipped with a rotating anode Cu target, was operated at 200 mA and 40 kV. The incident X-ray beam was monochromated by a pyrolytic graphite crystal, and a set of three pinhole inherent collimators were used so that the smearing effects inherent in slit-collimated small-angle X-ray cameras can be avoided. The scattered intensity was detected by a two-dimensional position-sensitive detector (ORDELA model 2201X, Oak Ridge Detector Laboratory Inc.) with 256 × 256 channels (active area 20 × 20 cm<sup>2</sup> with ~1 mm resolution). The sample-to-detector distance was 2100 mm long. The beam stop was a round lead disk of 18 mm in diameter. All data were corrected by the background (dark current and empty beam scattering) and the sensitivity of each pixel of the area detector. The area scattering pattern has been radially averaged to increase the photon counting efficiency compared with one-dimensional linear detector. The intensity profile was output as the plot of the scattering intensity ( $I$ ) vs the scattering vector,  $q = 4\pi/\lambda \sin(\theta/2)$  ( $\theta$  = scattering angle). All the intensity profiles reported here have also been corrected for thermal diffuse scattering (TDS). The intensity level of TDS was assumed to be a constant, and its magnitude was determined from the slope of the  $Iq^4$  vs  $q^4$  plot.<sup>21</sup>

Crystallization kinetics of PEO-*b*-PB/PB blends were studied by the isothermal crystallization experiments in a TA Instrument 2000 differential scanning calorimeter (DSC) equipped with the RCS cooling system. The temporal developments of crystallinity at various crystallization temperatures ( $T_c$ ) were monitored in this experiment. The sample was annealed at 80 °C for 2 min on a Linkam HFS 91 hot stage, followed by transferring into the DSC equilibrated at the desired  $T_c$  at which the isothermal crystallization was conducted. After the crystallization had proceeded for a specified time period,  $t$ , a DSC heating scan at 20 °C/min was immediately conducted to record the melting endotherm. The normalized crystallinity that had formed at time  $t$  was calculated by  $x_c(t) = \Delta h_f(t)/\Delta h_f(\infty)$ , with  $\Delta h_f(t)$  and  $\Delta h_f(\infty)$  being the enthalpy of melting measured after the crystallization had proceeded for time  $t$  and after it had reached the ultimate extent, respectively. This experiment was repeated for a sequence of  $t$  for each sample, so that the entire temporal development of crystallinity was followed.

## Results and Discussion

**Microdomain Morphology of PEO-*b*-PB/PB Blends in the Melt State.** The microphase-separated morphology of PEO-*b*-PB/PB in the melt state was probed by SAXS to verify the transformations of microdomain structures with PB concentration. Figure 1 displays the SAXS profiles of three representative compositions displaying the morphology of 1-D stacked lamellae ( $f_{PB} = 0.50$ ), hexagonally packed PEO cylinders

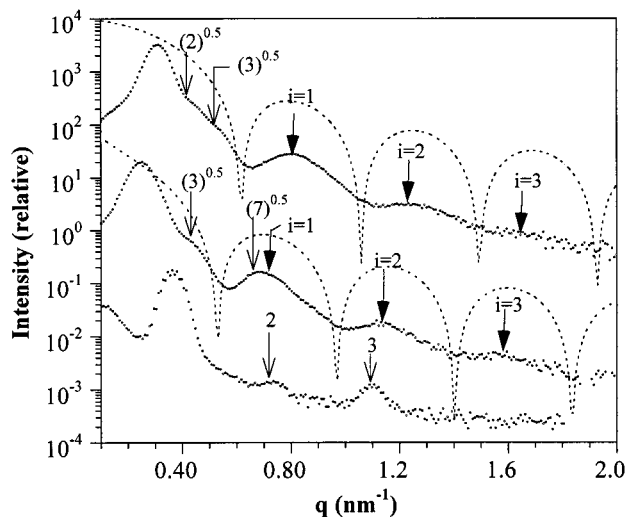


**Figure 1.** SAXS profiles of three representative compositions displaying the morphology of 1-D stacked lamellae ( $f_{PB} = 0.5$ ; the bottom curve), hexagonally packed PEO cylinders ( $f_{PB} = 0.78$ ; the middle curve), and bcc packed PEO spheres ( $f_{PB} = 0.83$ ; the top curve). The observed form factor peaks are denoted by “ $i = n$  ( $n = 1, 2, 3, \dots$ )”. The dashed lines signify the form factor scatterings of isolated cylinder and sphere calculated with the microdomain radii of 7.25 and 8.10 nm, respectively.

( $f_{PB} = 0.78$ ), and bcc packed PEO spheres ( $f_{PB} = 0.83$ ) in the melt. The dashed lines signify the form factor scatterings of isolated cylinder and sphere calculated with proper microdomain dimensions. From the relative positions of the lattice and form factor peaks, it is apparent that the three types of mesophases were accessible to PEO-*b*-PB through blending with low molecular weight PB homopolymers. The observed morphological transformations are 1-D stacked lamellae ( $0.5$  (neat PEO-*b*-PB)  $\leq f_{PB} < 0.69$ ), hexagonally packed PEO cylinder ( $0.69 \leq f_{PB} \leq 0.78$ ), and bcc packed PEO sphere ( $0.83 \leq f_{PB}$ ). The mesophases remained stable on heating to 150 °C. The disordered state was never accessed in the present study because the working temperatures were always lower than 80 °C.

**Nonisothermal Crystallization of PEO Blocks in PEO-*b*-PB/PB Blends.** Nonisothermal crystallization of the PEO blocks in PEO-*b*-PB/PB had been investigated in our previous study through the fixed cooling rate experiment.<sup>18</sup> The essential features observed are recalled here since they intimately connect with the present study. Figure 2 shows the DSC thermograms of the blends cooled at  $-5$  °C/min from 85 °C. The freezing temperature ( $T_f$ ) defined by the peak temperature of the crystallization exotherm is plotted against  $f_{PB}$  in the inset, and the important features are noted as follows: (1) the degree of undercooling ( $\Delta T = T_m^0 - T_f$ ;  $T_m^0 = 64$  °C)<sup>22</sup> required to initiate crystallization in the lamellar microdomains ( $\Delta T \approx 29$ – $39$  °C) is comparable to that associated with the PEO homopolymer ( $\Delta T \approx 24$  °C); (2) exceedingly large undercoolings are required for crystallizations in cylindrical ( $\Delta T \approx 90$  °C) and spherical ( $\Delta T \approx 96$  °C) microdomains; (3)  $T_f$  and hence the crystallization kinetics exhibit distinct transitions at the compositions corresponding to the morphological transformation. The third feature is particularly intriguing in that it demonstrates the feasibility of exploiting microdomain pattern to manipulate the crystallization kinetics of the block chains. Such a feasibility relies largely on a nucleation-controlled crystallization

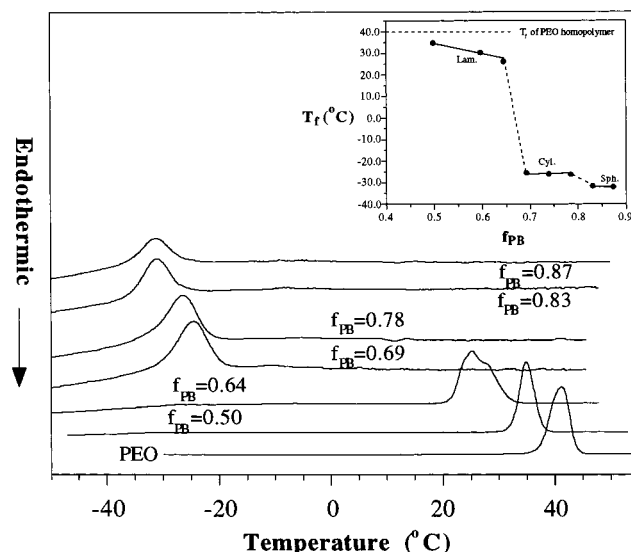


**Figure 2.** Nonisothermal crystallization exotherms of PEO-*b*-PB/PB blends. The cooling rate was 5 °C/min. The inset in the figure plots the freezing temperature ( $T_f$ ) as a function of  $f_{PB}$ . It can be seen that the crystallization kinetics exhibits transitions at the compositions corresponding to the morphological transformation.

in the individual microdomains, where the crystallization occurs through a slow homogeneous nucleation followed by the rapid growths of crystals to fill in the domain. The direct proportionality between homogeneous nucleation rate and domain volume<sup>23,24</sup> prescribes the tailor-made crystallization kinetics by the microdomain structures of the block copolymers.

Although homogeneous nucleation appears to be the plausible nucleation process in the microdomains, it is by no means the only allowable mechanism since heterogeneous nucleation may still be operative in a minor portion of microdomains having contact with the foreign particles (e.g., impurity particles and microvoids). These nucleation events, although only minor, may exert a drastic impact on the overall kinetics if the driving force of the subsequent crystal growth is capable of breaking out the melt morphology (e.g., in the weakly segregated systems with  $T_g$  of A blocks lower than the crystallization temperature).<sup>9,11</sup> In this case, the growth fronts will have a chance to thrust into the microdomains yet to be crystallized, and a repetitive intrusion will allow the crystals to grow over a macroscopic length scale from the heterogeneous nuclei. The crystallization will proceed as if the concentration discontinuity of the microdomains did not exist to frustrate the crystal growth so that it is initiated (via heterogeneous nucleation), propagated (via long-range crystal growth) and completed at the normal undercooling (i.e., the undercooling comparable to that of the homopolymer). Accordingly, the melt mesophase will be transformed into a lamellar morphology consisting of alternating crystalline and amorphous layers, and this has actually been observed in a number of systems such as PCL-*b*-PB<sup>8,20</sup> and PE-based block copolymers.<sup>10</sup>

For the crystallization in PEO-*b*-PB/PB blends, the large undercooling required in cylindrical and spherical morphology implies not only a homogeneous nucleation mechanism but also a highly frustrated crystal growth. On the contrary, crystallization in the lamellar melt should consist of a series of heterogeneous nucleation followed by the long-range crystal growth because the

crystallization can be initiated and completed at the normal undercooling. Crystal growths extending over hundreds of micrometers had actually been observed in the lamellar melt using polarized optical microscopy.<sup>18</sup>

A simple "self-seeding experiment" was employed to distinguish the length scales of crystal growth in the three mesophase structures. In this experiment, the crystalline sample was heated to a temperature,  $T_s$ , to melt the PEO crystals followed by immediate cooling at 5 °C/min to record the crystallization exotherm. If  $T_s$  is lower than the ultimate melting point of PEO ( $T_m^u$ ), a portion of crystals remains unmelted, and they serve as the nuclei from which crystal growth will start preferentially. If the crystal growth can advance over a macroscopic scale, the presence of these residual nuclei will inevitably promote the overall crystallization rate. Therefore, the samples heated to  $T_s < T_m^u$  will crystallize faster than those heated to  $T_s = T_m^u$ . On the other hand, if the crystal growth is highly frustrated, the residual nuclei remained in a small portion of microdomains will not assist the crystallization in the others. In this case, most microdomains still have to acquire new nuclei to initiate their own crystallizations, so that  $T_s$  will have no effect on the kinetics of the subsequent crystallization.

Figure 3 shows the DSC heating and subsequent cooling curves for the self-seeding experiments. It is clear for PEO homopolymer and the blend containing lamellar microdomains ( $f_{PB} = 0.64$ ) that  $T_s$  does affect the kinetics of the subsequent cooling crystallization. On the other hand, the crystallization kinetics of the compositions displaying cylindrical and spherical microdomains is hardly influenced by  $T_s$ . This simple experiment suggests that the crystal growth in lamellar melt could extend to the macroscopic scale, whereas that in the cylindrical and spherical morphology was highly frustrated.

**Isothermal Crystallization Kinetics and Crystalline Morphology.** In the bulk melt of homopolymers where crystal growth can advance freely over a macroscopic scale, both nucleation and crystal growth are operative simultaneously during the crystallization. The temporal development of crystallinity at a given temperature is properly described by the Avrami equation<sup>25</sup>

$$x_c(t) = 1 - \exp(-kt^n) \quad (1)$$

where  $x_c(t)$  is the normalized degree of crystallinity that has formed at time  $t$ ,  $k$  is the overall crystallization rate constant containing contribution from both nucleation and growth, and  $n$  is the Avrami exponent relating to the mechanism of nucleation as well as the growth geometry. Two nucleation mechanisms, viz. athermal and thermal nucleations, were considered in the formulation of the Avrami equation. In the case of athermal nucleation, the overall crystallization kinetics is governed by the rate of crystal growth because all nuclei were assumed to burst out at the onset of crystallization. The nuclei were assumed to be formed sporadically and randomly in space in thermal nucleation, so the kinetics is governed by the rates of both nucleation and growth.

Most homopolymers exhibit an Avrami exponent of  $n = 2-3$  which prescribes a sigmoidal shape in the plot of  $x_c(t)$  vs  $t$ . This sigmoidal shape should also apply to the C-A systems with crystallization proceeding through heterogeneous nucleation and long-range crystal growth.

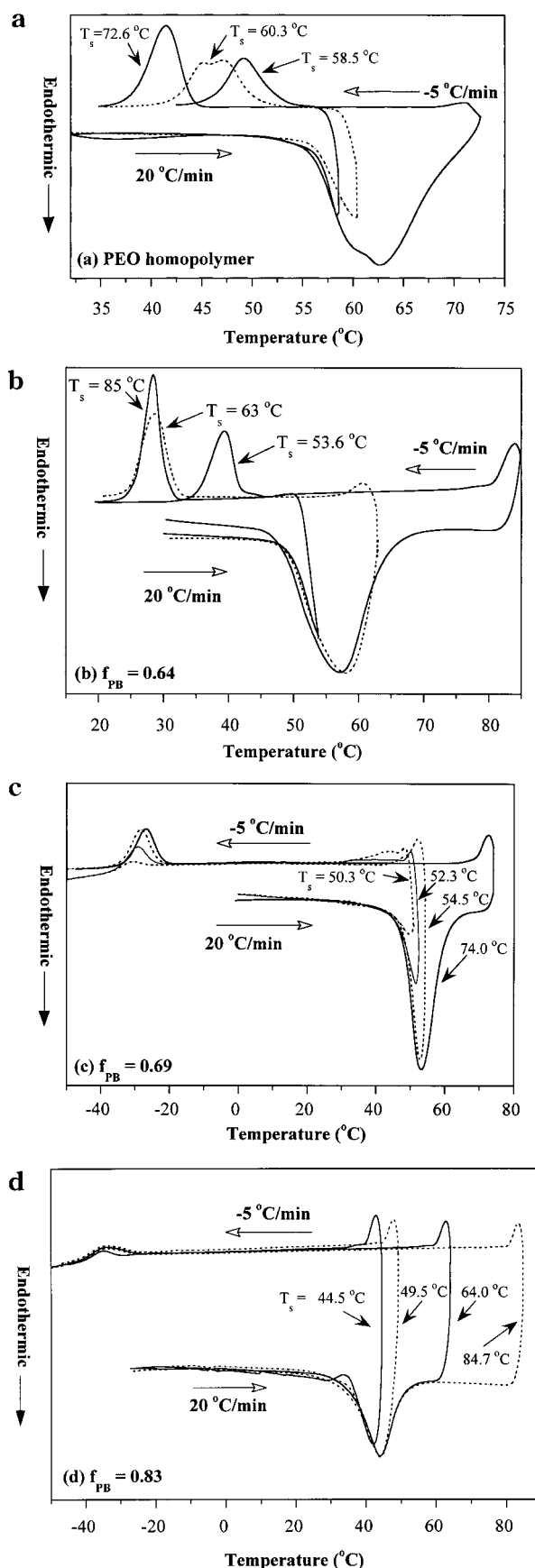


**Figure 3.** DSC heating (at 20 °C/min) and subsequent cooling (−5 °C/min) curves in the self-seeding experiments for (a) PEO homopolymer and PEO-*b*-PB/PB blends with (b)  $f_{PB} = 0.64$  (lamellar morphology in the melt state), (c)  $f_{PB} = 0.69$  (cylindrical morphology in the melt state), and (d)  $f_{PB} = 0.83$  (spherical morphology in the melt state).

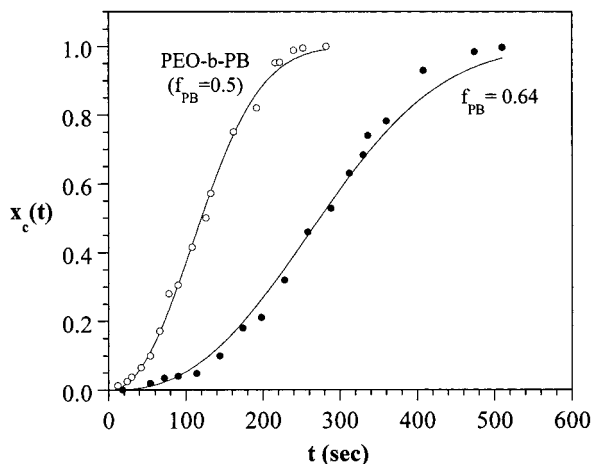


**Figure 4.** Developments of crystallinity during isothermal crystallizations in neat PEO-*b*-PB and a PEO-*b*-PB/PB blend with  $f_{PB} = 0.64$ . Both samples display lamellar morphology in the melt. The crystallization temperatures ( $T_c$ ) is 40 °C.

In the microphase-separated melt with crystal growth strongly frustrated by the nanoscaled continuity of microdomains, it can be assumed that once a nucleus is formed in a given microdomain, the subsequent growth pertaining to this nucleus is limited to a very short range such that it completes almost instantaneously before a new nucleus can be created in this microdomain.<sup>17</sup> This assumption is particularly sound when the nucleation occurs homogeneously, because the free energy barrier of homogeneous nucleation is much higher than that associated with crystal growth. Homogeneous nucleation, in this case, is always the rate-determining step in the crystallization.

In light of such a nucleation-controlled process, formulating the overall crystallization kinetics becomes straightforward. Analysis of the homogeneous nucleation rate at a given temperature by the first-order kinetics yielded the number fraction of homogeneous nuclei that has formed at time  $t$  ( $N(t)$ ) as<sup>23,24</sup>

$$N(t) = 1 - \exp(-k_N t) \quad (2)$$

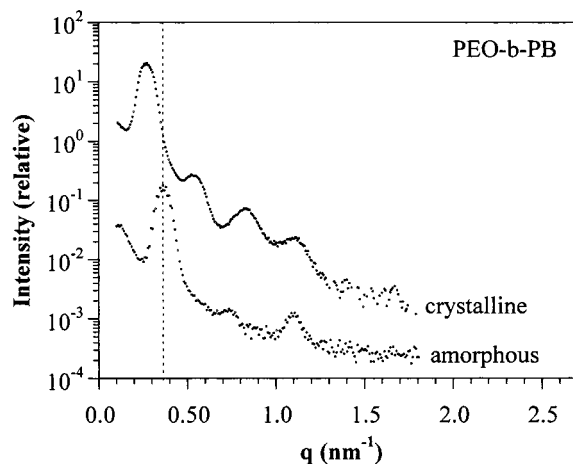
where  $k_N$  is the nucleation rate constant. If the crystal growth pertaining to each nucleus completes immediately after the nucleus has been formed,  $N(t) = x_c(t)$ ; substitution into eq 2 leads to

$$x_c(t) = 1 - \exp(-k_N t) \quad (3)$$

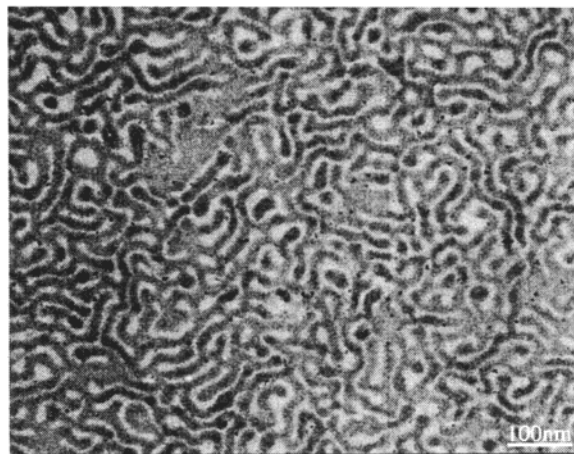
Equation 3 prescribes  $x_c(t)$  to follow a simple exponential function instead of a sigmoidal curve. This is the exponential function that described the crystallinity development in E/SEB reported by Loo et al.<sup>17</sup>

Figure 4 shows the developments of crystallinity in two compositions exhibiting lamellar morphology in the melt. The plot displays the sigmoidal shape properly fitted by the Avrami equation with  $n \approx 2.5$ . This verifies the foregoing suggestion that crystallization mechanism in the lamellar melt is essentially identical with the conventional spherulitic crystallization with long-range crystal growth from the heterogeneous nuclei.

Since the crystal growth is of long range, the original lamellar microdomains in the melt may have been perturbed to allow the repetitive intrusions of growth fronts. Such a morphological perturbation is plausible because the crystallization temperatures are far above



**Figure 5.** SAXS profiles of amorphous and crystalline PEO-*b*-PB. Both profiles display the multiple scattering maxima relevant to the lamellar morphology, but the peaks have shifted to lower  $q$  upon crystallization.



**Figure 6.** TEM micrographs showing the crystalline morphology of PEO-*b*-PB. The PB phase appears as the dark region due to staining by the OsO<sub>4</sub> vapor; the PEO phase is found as the gray interconnected lamellae.

the  $T_g$  of the PB phase and the interdomain distance in the lamellar melt is the shortest compared with those in cylindrical and spherical morphology. Figure 5 shows the SAXS patterns of the amorphous and crystalline PEO-*b*-PB. Both profiles display the multiple scattering maxima relevant to the lamellar morphology, but the peaks have shifted to lower  $q$  upon crystallization. The peak shift corresponds to an increase of interdomain distance from 17 to 22 nm, showing that the crystallization was not totally confined within the original microdomains. Figure 6 displays the real-space structure of the crystalline PEO-*b*-PB observed by transmission electron microscopy (TEM). It can be seen that the PEO lamellae (the gray regions) become tortuous and highly interconnected after crystallization. Such a highly interconnected structure is similar to that found in PEO-*b*-PI<sup>15</sup> and is in parallel with the suggestion that long-range crystal growth can be driven by the ability of the growth fronts to repeatedly invade into the microdomains yet to be crystallized.

Figure 7a presents the crystallinity development at various temperatures for a blend ( $f_{PB} = 0.69$ ) exhibiting cylindrical morphology in the melt. The curves are no longer sigmoidal but follow the exponential function prescribed by eq 3, as manifested from the linearity in

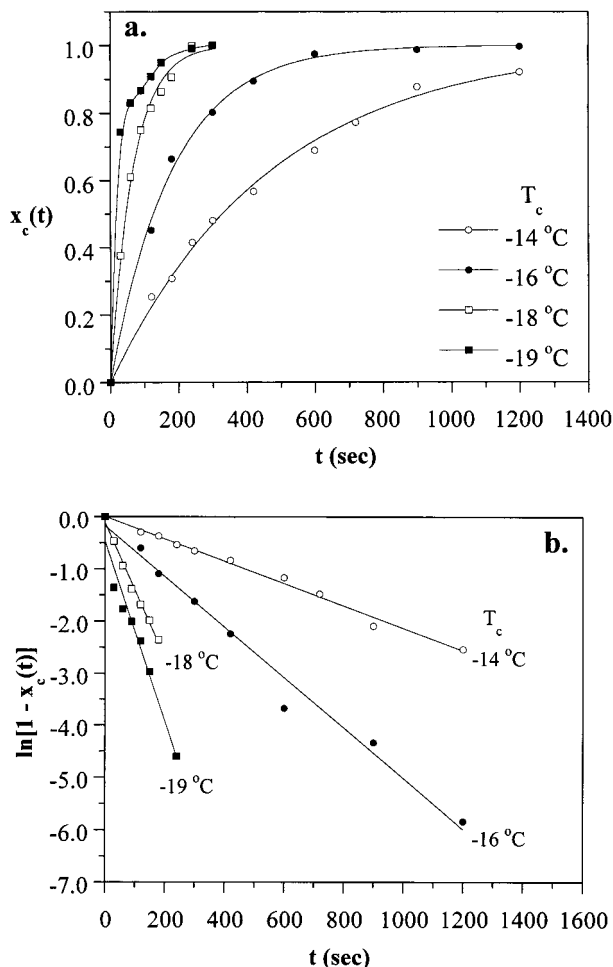


**Figure 7.** (a) Development of crystallinity during isothermal crystallization in a PEO-*b*-PB/PB with  $f_{PB} = 0.69$  (displaying cylindrical morphology in the melt state). (b) The corresponding  $\ln[1 - x_c(t)]$  vs  $t$  plot showing a good linearity. The crystallization temperatures are indicated in the figure.

$\ln[1 - x_c(t)]$  vs  $t$  plots in Figure 7b. The exponential development of crystallinity plus the exceedingly large undercoolings asserts that the crystallization kinetics in cylindrical morphology is controlled by homogeneous nucleation.

As the crystal growth is highly frustrated in the cylindrical morphology, we may expect the melt structure to be largely retained upon crystallization because the repetitive intrusion of growth fronts is either prohibited or ineffective. Figure 8 shows the SAXS profiles of the amorphous and crystalline blend with  $f_{PB} = 0.69$ . Interestingly, the melt structure is not totally preserved as the scattering peaks have shifted to lower  $q$  and broadened upon crystallization. The crystalline morphology does not seem to be 1-D stacked lamellae either judging from the fact that the relative positions of the primary peak and of the vaguely defined higher-order peaks (appearing as shoulders) do not appear to follow the ratio characteristic to a lamellar morphology.

To verify the postulate that the crystalline morphology is neither 1-D stacked lamellae nor identical with the melt structure, we proceed to determine the specific surface area ( $S/V$ ;  $S$  and  $V$  being the total surface area of the phase boundary and the total volume of the system, respectively) using the intensity profile at the tail region. According to the Porod law for a two-phase

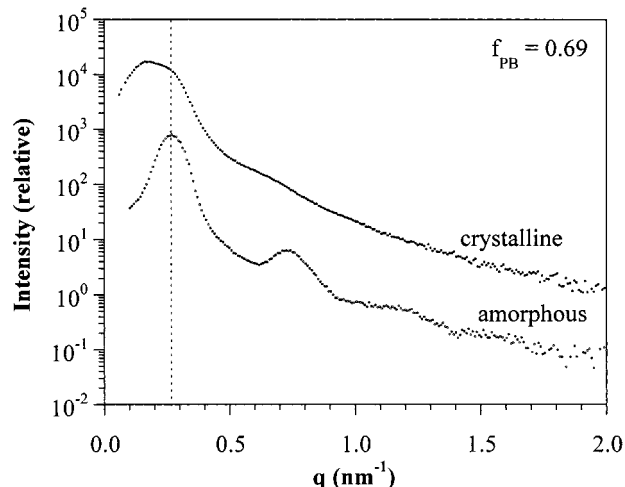


**Figure 8.** SAXS profiles of the amorphous and crystalline blend with  $f_{PB} = 0.69$ . It can be seen that the scattering peaks have shifted to lower  $q$  and broadened upon crystallization.

system, the asymptotic behavior of scattering intensity is given by<sup>26</sup>

$$\frac{I(q)}{Q} = \frac{2\pi(S)}{f_1 f_2 (V)} \frac{1}{q^4} \quad (4)$$

where  $Q$  is the invariant and  $f_i$  is the volume fraction of phase  $i$ . The values of  $S/V$  may in principle be determined from the plateau observed at the tail region of  $Iq^4/Q$  vs  $q$  plot. This method however suffers uncertainties arising from the maxima and oscillations in the scattering curve due to interdomain and intradomain interferences, as well as the effect of the finite thickness of the interfacial boundary. These uncertainties, as pointed out by Micha et al., can be circumvented by the use of correlation functions.<sup>27</sup> The 3-D Fourier transform of eq 4 yields the correlation function at small radial distance  $r$  as<sup>26,27</sup>

$$\gamma(r) = 1 - \frac{r}{l_p} \quad (5)$$

where  $l_p$  is the Porod length given by

$$\frac{1}{l_p} = \frac{1}{4f_1 f_2} \left( \frac{S}{V} \right) \quad (6)$$

Figure 9 displays the representative  $\gamma(r)$  of a crystalline sample with  $f_{PB} = 0.69$ .  $l_p$  can be determined from the slope of the linear region occurred at small  $r$  ( $1 \text{ nm} < r < 5 \text{ nm}$  in the present case), and  $S/V$  can be calculated from  $l_p$  accordingly.

Table 1 lists the values of the observed  $S/V$  of the amorphous and crystalline samples. For the amorphous samples displaying cylindrical morphology,  $S/V$  is related to the radius of the cylinder ( $R_{\text{cyl}}$ ) through

$$\frac{S}{V} \cong \frac{2f_{\text{PEO}}}{R_{\text{cyl}}} \quad (7)$$

The average  $R_{\text{cyl}}$  calculated from the above formula is 7.0 nm, in good agreement with that (7.25 nm) determined from the positions of the form factor peaks.

We now compare the observed  $S/V$  of the crystalline samples with the  $S/V$  calculated by assuming the following two extreme conditions:

**Table 1. Specific Surface Areas ( $S/V$ ) of Amorphous and Crystalline PEO-*b*-PB/PB Blends**

$f_{PB}$	physical state of PEO blocks	$q_{max}$ (nm <sup>-1</sup> )	$q_{max}^{L-C}$ (nm <sup>-1</sup> )	obsd $S/V$ (nm <sup>-1</sup> )	$(S/V)_{lam}$ (nm <sup>-1</sup> )	$(S/V)_{hex}$ (nm <sup>-1</sup> )	$(S/V)_{bcc}$ (nm <sup>-1</sup> )
0.50	amorphous		0.371	0.127	0.118		
	crystalline		0.286	0.098	0.091		
0.60	amorphous		0.352	0.121	0.112		
	crystalline		0.258	0.085	0.082		
0.69	amorphous	0.272		0.085		0.080	
	crystalline	0.176	0.267	0.070	0.085	0.051	
0.74	amorphous	0.268		0.074		0.072	
	crystalline	0.190	0.226	0.061	0.072	0.050	
0.78	amorphous	0.252		0.066		0.062	
	crystalline	0.149	0.198	0.050	0.063	0.036	
0.83	amorphous	0.278		0.062			0.059
	crystalline	0.197	0.213	0.050	0.068		0.041

<sup>a</sup>  $q_{max}$  and  $q_{max}^{L-C}$  are the positions of the primary SAXS peaks observed in  $I$  vs  $q$  and Lorentz-corrected  $Iq^2$  vs  $q$  profiles, respectively. <sup>b</sup>  $(S/V)_{lam}$  is the specific surface area calculated by assuming that the morphology giving rise to the observed scattering profile is the 1-D stacked lamellae. <sup>c</sup>  $(S/V)_{hex}$  is the specific surface area calculated by assuming that the morphology giving rise to the observed scattering profile is the hexagonally packed cylinders. <sup>d</sup>  $(S/V)_{bcc}$  is the specific surface area calculated by assuming that the morphology giving rise to the observed scattering profile is the bcc packed spheres.

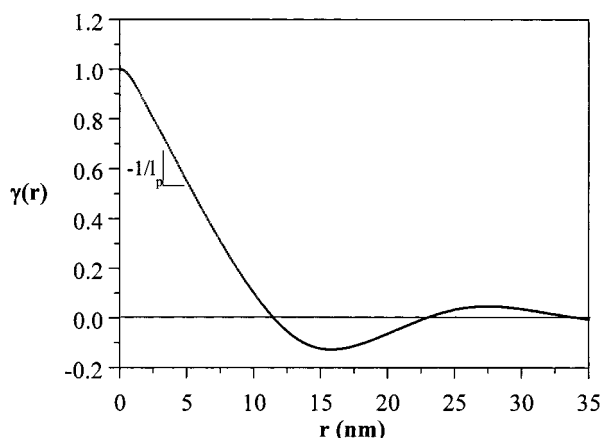


**Figure 9.** A representative correlation function showing the determination of the Porod length ( $l_p$ ) from the slope of the linear region occurred at small  $r$ .

(1) Crystallization totally disrupted the original long-range order and cylinder structure in the melt and transformed the morphology into 1-D stacked lamellae with large lateral dimensions; the resultant lamellar morphology then gave rise to the SAXS patterns observed in Figure 8. The corresponding  $S/V$  is given by

$$\left(\frac{S}{V}\right)_{lam} = \frac{2}{L} \quad (8)$$

where  $L$  is the interdomain distance in the 1-D array calculated from the peak position ( $q_{max}^{L-C}$ ) of the "Lorentz-corrected" ( $Iq^2$  vs  $q$ ) profile, viz.  $L = 2\pi/q_{max}^{L-C}$ .

(2) The hexagonal packing was still retained upon crystallization; the resultant morphology (i.e., hexagonally packed "crystalline cylinders") then gave rise to the SAXS profiles observed in Figure 8. The corresponding  $S/V$  in this case is given by

$$\left(\frac{S}{V}\right)_{hex} = \frac{2f'_{PEO}}{R_{cyl}} = \frac{2\sqrt{f'_{PEO}}}{D} \left(\frac{2\pi}{\sqrt{3}}\right)^{1/2} \quad (9)$$

where  $f'_{PEO}$  is the volume fraction of PEO phase after crystallization (calculated with the knowledge of crystallinity),<sup>29</sup>  $R_{cyl}$  is the average radius of the crystalline cylinder, and  $D$  is the average interdomain distance

calculated from the position of the first peak ( $q_{max}$ ) in Figure 8, viz.<sup>30</sup>

$$D = \sqrt{\frac{4}{3}} \frac{2\pi}{q_{max}} \quad (10)$$

Equation 9 was derived through the following relation between  $R_{cyl}$  and  $D$  for a hexagonal lattice:<sup>30</sup>

$$R_{cyl} = \left(\frac{\sqrt{3}f'_{PEO}}{2\pi}\right)^{1/2} D \quad (11)$$

The calculated values of  $(S/V)_{lam}$  and  $(S/V)_{hex}$  are also listed in Table 1. It should be noted that the  $S/V$  evaluated from the above two cases implicitly assumed idealized lamellar and hexagonally packed cylinder morphology with uniform interdomain distances prescribed by the positions of the observed SAXS peaks. For the compositions ( $f_{PB} = 0.69$ – $0.78$ ) considered now, the ideal hexagonally packed cylinder morphology applies well to the melt state in that the observed  $S/V$  of the amorphous samples agrees well with the corresponding  $(S/V)_{hex}$  (Table 1). Deviation of the observed  $S/V$  from the calculated  $(S/V)_{hex}$  simply suggests that the morphology deviates from the ideal type of morphology the system exhibits in the melt state.

It can be seen from Table 1 that the difference between the observed  $S/V$  and the corresponding  $(S/V)_{lam}$  is more than 20% for the three crystalline samples ( $f_{PB} = 0.69$ ,  $0.74$ , and  $0.78$ ) displaying cylindrical morphology in the melt. This large discrepancy strongly suggests that the melt structure was not transformed into one-D stacked lamellae as found in a number of systems. This reconciles with the large undercooling observed in the crystallization kinetics study, because the crystallization would have started and completed at the normal undercooling if such a long-range disruption were accessible.

The difference between the observed  $S/V$  and the corresponding  $(S/V)_{hex}$  is also over 20%, suggesting that the hexagonally packed cylinder morphology in the melt is not totally preserved either. As the melt morphology is neither totally disrupted (into lamellar morphology) nor fully preserved (as hexagonally packed crystalline cylinders), it is likely that some intermediate structures have been generated through the crystallization. Considering the observed  $S/V$  of the crystalline samples is about 18% lower than that of the corresponding amor-

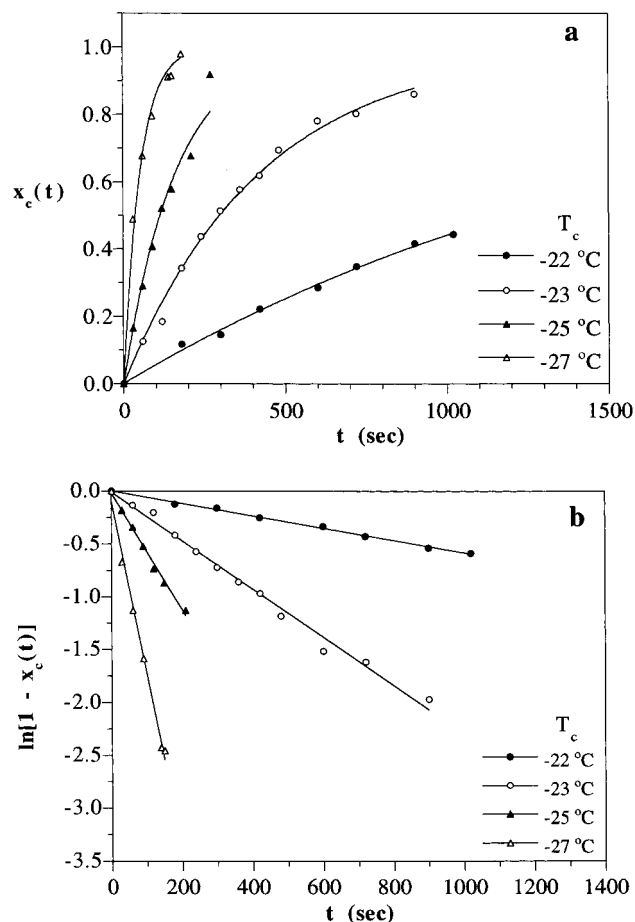


**Figure 10.** (a) Development of crystallinity during isothermal crystallization in a PEO-*b*-PB/PB with  $f_{PB} = 0.83$  (displaying spherical morphology in the melt state). (b) The corresponding  $\ln[1 - x_c(t)]$  vs  $t$  plot showing a good linearity. The crystallization temperatures are indicated in the figure.

phous samples, the intermediate structure was probably formed through some short-range coalescence of the PEO cylinders. Such a short-range coalescence could be driven by the intrusions of the growth fronts into the nearby microdomains or occurred through some other mechanisms. TEM experiments are currently underway to reveal the real-space morphology of the intermediate structure and the mechanism associated with the structural formation.

The temporal development of crystallinity in the PEO spheres is shown in Figure 10. The curves also follow the exponential function prescribed by eq 3, thus verifying a homogeneous nucleation controlled crystallization in the spherical morphology.

Figure 11 presents the SAXS profiles of the amorphous and crystalline blends with  $f_{PB} = 0.83$ . The melt structure is again not totally preserved as the scattering peaks also shift to lower  $q$  upon crystallization. The specific surface areas calculated from the correlation function are also tabulated in Table 1 along with the calculated  $(S/V)_{lam}$  and  $(S/V)_{bcc}$ .  $(S/V)_{bcc}$  is the specific surface area expected when the bcc long-range order is retained upon crystallization; it was calculated through the following formula for the bcc lattice:<sup>30</sup>

$$\left(\frac{S}{V}\right)_{bcc} = \frac{3f'_{PEO}}{R_{sph}} = \frac{3f'_{PEO}}{D} \left(\frac{\sqrt{3}\pi}{f'_{PEO}}\right)^{1/3} \quad (12)$$

where  $R_{sph}$  is the radius of the crystalline sphere and

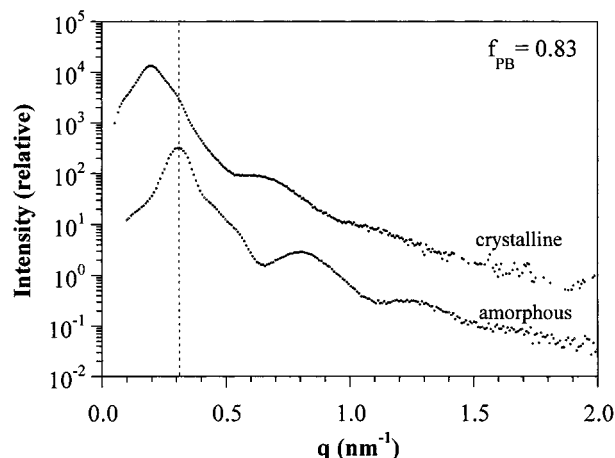


**Figure 11.** SAXS profiles of the amorphous and crystalline blend with  $f_{PB} = 0.83$ . It can be seen that the scattering peaks have shifted to lower  $q$  and broadened upon crystallization.

$D$  is the interdomain distance calculated from the position of the first SAXS peak via

$$D = \sqrt{\frac{3}{2}} \frac{2\pi}{q_{max}} \quad (13)$$

It can be seen in Table 1 that the lamellar morphology was not formed upon crystallization since the difference between the observed  $S/V$  and the calculated  $(S/V)_{lam}$  is 36%. The original bcc packing was not preserved either as the observed  $S/V$  is apparently 18% larger than the corresponding  $(S/V)_{bcc}$ . These discrepancies again suggest that crystallization probably transformed the melt mesophase into some structures intermediate to the 1-D stacked lamellae and bcc packed crystalline spheres.

## Conclusions

The crystallization kinetics and crystalline morphology of PEO-*b*-PB/PB blends have been studied. Crystallization of PEO blocks in the lamellar melt was analogous to the common spherulitic crystallization in homopolymers where the process occurred through a series of heterogeneous nucleations followed by the propagation of crystal growth over a macroscopic scale. The crystal growth was of long range because the growth fronts could repeatedly thrust into the microdomains yet to be crystallized, and such a repetitive intrusion generated a highly interconnected lamellar morphology. The crystallinity developments in the blends containing cylindrical and spherical microdomains followed the first-order kinetics as anticipated when the crystallization was controlled by homogeneous nucleation. Under the prescribed nonisothermal crystallization, the corresponding melt structures were neither totally disrupted into a lamellar morphology nor fully preserved upon crystallization. It was likely that some intermediate structures had been generated through the crystallizations. Further studies are underway to reveal the real-space morphology of the intermediate structures and the mechanisms associated with the structural formation.

**Acknowledgment.** We thank Mr. Kazuhiro Yamachi at Professor Takeji Hashimoto's lab for kindly conducting the TEM experiment. This work was supported by the National Science Council of R.O.C. under

Grant NSC 89-2216-E-007-048 and also in part by the U.S. Department of Energy under Contract DE-AC05-00OR22725 with the Oak Ridge National Laboratory, managed by the UT-Battelle, LLC.

## References and Notes

- (1) Leibler, L. *Macromolecules* **1980**, *13*, 1602.
- (2) Hashimoto, T.; Shibayama, M.; Fujimura, M.; Kawai, H. In *Block Copolymers—Science and Technology*; Meier, D. J., Ed.; Harvard Academic Publishers: London, 1983.
- (3) Bates, F. S.; Fredrickson, G. H. *Phys. Today* **1999**, *52*, 32.
- (4) Hamley, I. W. *The Physics of Block Copolymers*; Oxford University Press: New York, 1998; Chapter 5.
- (5) DiMarzio, E. A.; Guttman, C. M.; Hoffman, J. D. *Macromolecules* **1980**, *13*, 1194.
- (6) Whitmore, M. D.; Noolandi, J. *Macromolecules* **1988**, *21*, 1482.
- (7) Nojima, S.; Kato, K.; Yamamoto, S.; Ashida, T. *Macromolecules* **1992**, *25*, 2237.
- (8) Nojima, S.; Nakano, H.; Ashida, T. *Polymer* **1993**, *34*, 4168.
- (9) Rangarajan, P.; Register, R. A.; Fetters, L. J.; Naylor, S.; Ryan, A. J. *Macromolecules* **1995**, *28*, 1422.
- (10) Ryan, A. J.; Hamley, I. W.; Bras, W.; Bates, F. S. *Macromolecules* **1995**, *28*, 3860.
- (11) Ryan, A. J.; Fairclough, J. P. A.; Hamley, I. W.; Mai, S.-M.; Booth, C. *Macromolecules* **1997**, *30*, 1723.
- (12) Zhu, L.; Chen, Y.; Zhang, A.; Calhoun, B. H.; Chun, M.; Quirk, R. P.; Cheng, S. Z. D.; Hsiao, B. S.; Yeh, F.; Hashimoto, T. *Phys. Rev. B* **1999**, *60*, 10022.
- (13) Lotz, B.; Kovacs, A. J. *ACS Polym. Prepr.* **1969**, *10*, 820.
- (14) Robitaille, C.; Prud'homme, J. *Macromolecules* **1983**, *16*, 665.
- (15) Schnablegger, H.; Rein, D. H.; Rempp, P.; Cohen, R. E. *J. Polym. Eng.* **1996**, *16*, 1.
- (16) Weimann, P. A.; Hajduk, D. A.; Chu, C.; Chaffin, K. A.; Brodil, J. C.; Bates, F. S. *J. Polym. Sci., Polym. Phys. Ed.* **1999**, *37*, 2053.
- (17) Loo, Y.-L.; Register, R. A.; Ryan, A. J. *Phys. Rev. Lett.* **2000**, *84*, 4120.
- (18) Chen, H.-L.; Hsiao, S.-C.; Lin, T.-L.; Yamauchi, K.; Hasegawa, H.; Hashimoto, T. *Macromolecules* **2001**, *34*, 671.
- (19) Nojima, S.; Nakano, H.; Takahashi, Y.; Ashida, T. *Polymer* **1994**, *35*, 3479.
- (20) Nojima, S.; Yamamoto, S.; Ashida, T. *Polym. J.* **1995**, *27*, 673.
- (21) Medellin-Rodriguez, F. J.; Philips, P. J.; Lin, J. S. *Macromolecules* **1996**, *29*, 7491.
- (22) Point, J. J. *Macromolecules* **1997**, *30*, 1375.
- (23) Turnbull, D.; Cormia, R. L. *J. Chem. Phys.* **1961**, *34*, 820.
- (24) Cormia, R. L.; Price, F. P.; Turnbull, D. *J. Chem. Phys.* **1962**, *37*, 1333.
- (25) Avrami, M. *J. Chem. Phys.* **1939**, *7*, 1103.
- (26) Porod, G. *Kolloid Z. Z. Polym.* **1951**, *124*, 83; **1952**, *125*, 51; **1952**, *125*, 108.
- (27) Micha, M. A.; Burger, C.; Antonietti, M. *Macromolecules* **1998**, *31*, 5930.
- (28) Roe, R.-J. *Methods of X-ray and Neutron Scattering in Polymer Science*; Oxford University Press: New York, 2000.
- (29)  $f'_{\text{PEO}} = (w_{\text{PEO}}/\rho_{\text{PEO}}^x) / [w_{\text{PEO}}/\rho_{\text{PEO}}^x + (1 - w_{\text{PEO}})/\rho_{\text{PB}}]$ , where  $w_{\text{PEO}}$  is the overall weight fraction of PEO,  $\rho_{\text{PB}}$  is the density of PB, and  $\rho_{\text{PEO}}^x$  is the density of the crystalline microdomains.  $\rho_{\text{PEO}}^x$  is given by  $\rho_{\text{PEO}}^x = \rho_{\text{a,PEO}} + \phi_c(\rho_{\text{c,PEO}} - \rho_{\text{a,PEO}})$ , where  $\rho_{\text{a,PEO}}$  and  $\rho_{\text{c,PEO}}$  are the amorphous and crystalline densities of PEO, respectively, and  $\phi_c$  is the volume fraction crystallinity in terms of per unit volume of PEO microdomains. The values of densities used are  $\rho_{\text{a,PEO}} = 1.12 \text{ g/cm}^3$ ,  $\rho_{\text{c,PEO}} = 1.24 \text{ g/cm}^3$ , and  $\rho_{\text{PB}} = 0.94 \text{ g/cm}^3$ .
- (30) Tanaka, H.; Hasegawa, H.; Hashimoto, T. *Macromolecules* **1991**, *24*, 240.

MA010552H